(Received 28 March 2025, Accepted 21 April 2025, Scheduled 11 May 2025)

Compact Quadband NGD Microstrip Circuit for 2–6 GHz ISM Bands

Nathan B. Gurgel[1], Glauco Fontgalland[2], Idalmir S. Queiroz Jr.[3], Samanta M. Holanda[3], Benoit Agnus[4], Jerome Rossignol[5], and Blaise Ravelo[6,*]

[1] *Applied Electromagnetic and Microwave Laboratory, Federal University of Campina Grande, Campina Grande 58429, Brazil*
[2] *Brenton School of Engineering, University of Mount Union, Alliance, OH 44601, USA*
[3] *Engineering and Technology Department, Federal Rural University of Semi Arid, Mossoró 59625900, Brazil*
[4] *SCIENTEAMA, 4 Avenue de Cambridge, 14200 Herouville Saint Clair, France*
[5] *Université de Bourgogne, Dijon, France*
[6] *School of Electronic & Information Engineering, Nanjing University of Information Science & Technology (NUIST) Nanjing 210044, Jiangsu, China*

ABSTRACT: With the increasing interest in negative group delay (NGD) function for RF and microwave circuits, and sensing applications, techniques to fit multiple NGD bands in a single and compact structure can open new possibilities. In this work, a simple and innovative compact quadband NGD microstrip circuit is presented for all ISM bands between 2 GHz and 6 GHz. The circuit is composed of a base line (BL) coupled to the transmission line, which sets the lowest NGD band, and each additional NGD band is created by inserting stubs into the BL. The impact of each stub on the overall circuit is analyzed using parametric simulation. The design and tuning method of the coupled line used to achieve the NGD multiband function is described in detail. Through the insertion loss and group delay results, a well-fitted correlation is observed between the simulated and measured results, where the simulated transmission coefficient and group delay show NGD quadband response with center frequencies at 2.46, 3.49, 4.96, and 5.69 GHz with respective NGD bandwidth of 0.89%, 0.83%, 0.66%, and 0.97%, respectively, whereas the measured results present center frequency NGD deviation of less than 1%. In addition, the NGD quadband circuit prototype has a compact size $40.2 \times 30.2 \times 1.57\,\text{mm}^3$. The measured NGD results are in good agreement with simulated ones.

1. INTRODUCTION

Counterintuitive by nature for "advancing" signal in time [1], the negative group delay (NGD) effect brings a new opportunity to address real time systems, signal integrity, filtering, and other microwave area problems due to its effect of phase correction without adding more signal delay to it. The NGD function finds a myriad of useful applications throughout the literature such as in antenna arrays [2–5], phase shifters [6–9], sensors prediction [10–13], power dividers [14–17], and bandpass (BP) filters signal linearization [18–20] where some cases are based on coupled lines (CLs) [2, 3, 14, 18–20] guaranteeing a good fine-tuning process through simulations and enhanced NGD per ratio of transmission coefficient, compared to lumped NGD circuits.

Despite having interesting results, for multiband purposes NGD distributed circuits occupy a wide area due to the necessity of multiple CLs, thus recent studies have focused on developing new topologies to address this situation [18–29]. In [18–20], different topologies to create a dual-band NGD circuit inside a bandpass filter were proposed to have a flat group delay behavior, but to achieve this it was used six terminated, four and two terminated CLs along the filter, and for the last ones, a consideration of triple CLs phenomenon is required to achieve the linearization with an Insertion Loss (IL) of less than 2 dB.

In [21], a dual-band NGD circuit comprising frequencies at 2.3 and 2.86 GHz with the NGD values of -8.1 and -1.84 ns, respectively, was achieved using a "lill" shaped topology which is built using one two-port transmission line coupled to three open stub lines, alas no parameterization analysis was done. Better comprehension of the multicoupled technique can be seen in [22] where a topology resembling a bar code was used to achieve a triband NGD between 2.1 and 2.6 GHz. Although successful in achieving, the problem dealing with multicoupling needs to be solved up to 80 MHz deviation between the simulated and measured NGD center frequencies.

To address the multicoupling problem, a dual-band technique based on two CLs located at both sides of the transmission line (TL) is shown in [24]. The two CLs give a good isolation in the two NGD bands, thus enabling easy tuning process. This is especially useful when dealing with only two bands, but no generalization of this technique is presented in the work.

Other authors approached multiband NGD behavior by utilizing defected structures [26–29], but we could raise a critic of whether these bands are independent modes or are just harmonics. Especially for [27–29], the NGD behaviors are obtained with most possible harmonics since the transmission coefficient, S_{21}, presents only a second order equation, and no

* Corresponding author: Blaise Ravelo (blaise.ravelo@yahoo.fr).

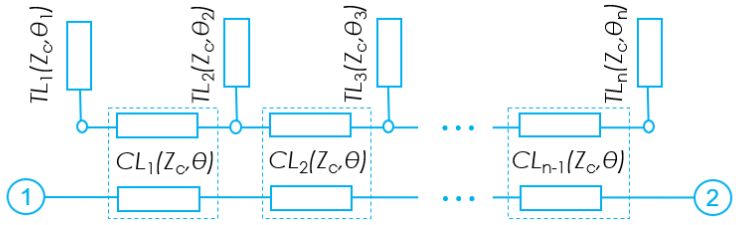

FIGURE 1. Multiband NGD distributed topology.

FIGURE 2. Two-port S-parameter black box model.

electrical current analysis shows the same path for most bands. In [26], the multibands are achieved by switching resistors, which causes a change of current path and consequently the behavior of the NGD response.

In this work, we present a quadband NGD circuit based on what we call "crown" topology, which is built upon a commensurate line circuit form for a CL ladder topology filter which acts as a reject band filter. Using a base CL as the lowest out-of-band region filter, we add new open stubs so that new resonance regions are created between the interaction of these new stubs and the base CL, thus occupying less space than conventional circuit based on multiple CLs. We show by electrical current density analysis that each region is an independent mode, and we can easily tune each region by a simple iterative process. The main research contribution of the present study for the NGD microwave engineering is on:

- The design method of quadband NGD microstrip circuits in the challenging ISM bands from 2 GHz to 6 GHz and
- The S-parameters and group delay (GD) global modelling methodology based on CL ladder topological approach.

This work is organized as follows.

- Section 2 theoretically describes how the multiband NGD circuit works, establishing fundamental equations that describe its functionality.
- Section 3 focuses on the quadband NGD proof of concept (POC) implemented with microstrip technology. The main concept of low coupling between the different modes generated by the NGD topology is studied by High Frequency Simulation Software (HFSS®) electromagnetic (EM) simulations.
- Section 4 investigates the parameterization of the "Crown" topology by showing the influences and presenting the main concept of low coupling between each mode.
- Section 5 discusses the simulated and measured results and comparison with recent literature.
- Section 6 is the conclusion of the paper, elucidating the main points of the development.

2. THEORETICAL ANALYSIS OF MULTIBAND NGD TOPOLOGY

The multiband NGD topology is theoretically studied in this section.

2.1. Description of Multiband NGD Topology

For the analytical approach of the proposed crown topology, consider the two-port distributed structure shown in Fig. 1. The present topology is constituted by n stubs of open-ended transmission lines (TLs) $\mathrm{TL}_{m=1,2,\ldots n}(Z_c, \theta_m)$ with identical characteristic impedance Z_c and electrical lengths $\theta_{m=1,2,\ldots n}$ which are connected to CLs $\mathrm{CL}_{m=1,2,\ldots n-1}(Z_c, \theta)$.

In the other words, the TLs are coupled to a multi-resonator by coupling factor $k_{m=1,2,\ldots n-1}$ stubs attached to it. The resonator possesses m stubs attached to it. For simplicity, the stubs are uncoupled.

2.2. S-Parameter Approach and GD Analysis

As seen in Fig. 2, the crown topology can be modelled from impedance matrix $[Z_{NGD}(s)]$ with $s = j\omega$ (ω is the angular frequency) being the Laplace variable.

For the case of the proposed study, since the analysis is done on impedance, a Z-to-S conversion is necessary to determine the S-parameter model with R representing the reference characteristic impedance. It implies the S-parameter model. In the case of symmetric ports where they have the same characteristic impedance, we have reflection coefficients $S_{11} = S_{22}$ in addition to transmission coefficients $S_{12} = S_{21}$.

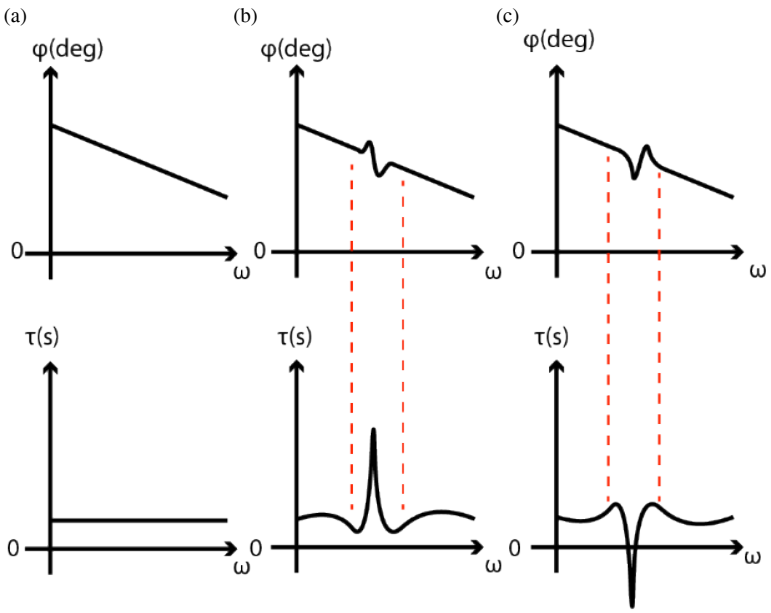

FIGURE 3. (a) Constant GD, (b) PGD and (c) NGD frequency responses of phase and GD.

The GD parameter relates the phase transition for each angular frequency and is given by:

$$\tau(\omega) = \frac{-d\phi(\omega)}{d\omega} \tag{1}$$

where $\phi(\omega) = \angle S_{NGD21}(j\omega)$ is the phase of transmission coefficient S_{NGD21}. Depending on the medium, the signal has an expected phase deviation. For lossless medium, a constant GD ($\tau = cte$) is expected. For lossy medium, we have both positive GD (PGD), $\tau > 0$, and NGD, $\tau < 0$. For a better comprehension of this phenomenon, see Fig. 3.

In brief, the NGD analysis consists in determining the circuit parameters allowing to reach the negative condition $\tau(\omega) < 0$. In other words, to present NGD, the ratio between the imaginary part of the denominator of S_{21} and its derivative must be greater than its real counterpart.

To address the circuit's NGD bandwidth (BW) control, let us evaluate the simplest model, which is made by a single coupled line and two stubs. The NGD bandwidth of the circuit is given by:

$$\mathrm{BW_{NGD}}(\%) = 100 \times \frac{\omega_2 - \omega_1}{\omega_0} \tag{2}$$

with the NGD center frequency $f_0 = \omega_0/(2\pi)$ defined by:

$$\tau(\omega_0) = \tau_{\min} \tag{3}$$

As underlined in [32], the proposed NGD BW is different from the 3-dB one related to magnitude because the cut-off frequencies ($\omega_1 < \omega_2$) are defined as the root of equation:

$$\begin{cases} \tau(\omega_1) = 0 \\ \tau(\omega_2) = 0 \end{cases} \tag{4}$$

The design and tuning procedure of the proposed quadband NGD circuit by electromagnetic (EM) simulation is described in the following subsection.

2.3. Quadband NGD Circuit Tuning Procedure

It is possible to determine the quadband NGD circuit design procedure to develop an arbitrary multiband filter organized in 5 steps as follows:

- Step 1: Model the base CL to resonate at the lowest frequency.
- Step 2: Add one stub at the center of the circuit.
- Step 3: Adjust the length of the stub to match the frequency of interest.
- Step 4: If coupling is present, reduce the length of the stubs of the affected frequencies, starting with the outermost and going to the innermost until satisfied.
- Step 5: Repeat steps 2 to 4 until all BWs are achieved.

The performance of the multiband NGD circuit will be analyzed when the dimension parameters of the circuit are changed. To validate the NGD theory, the POC design is discussed in the next section.

3. DESIGN AND EM SIMULATION OF QUADBAND NGD MICROSTRIP POC

This section focuses on the quadband NGD POC design investigation via surface current HFSS simulations.

3.1. Description of Quadband NGD Microstrip POC

To test the hypothesis, the quadband NGD circuit depicted in Fig. 4 is proposed. The quadband NGD prototype is implemented on a substrate with 1.52 mm thick Rogers RT Duroid 5880 ($\epsilon_r = 2.2$) and 35 µm double cladded copper.

It is made of a TL coupled to a base CL of length L_{CL} with five stubs where each one has a height H_n and same width

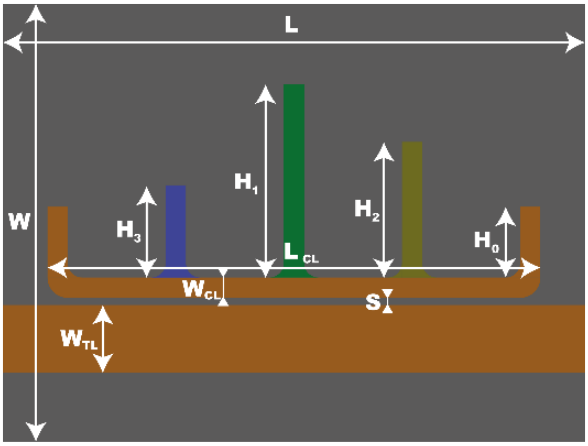

FIGURE 4. HFSS® design of the quadband NGD circuit.

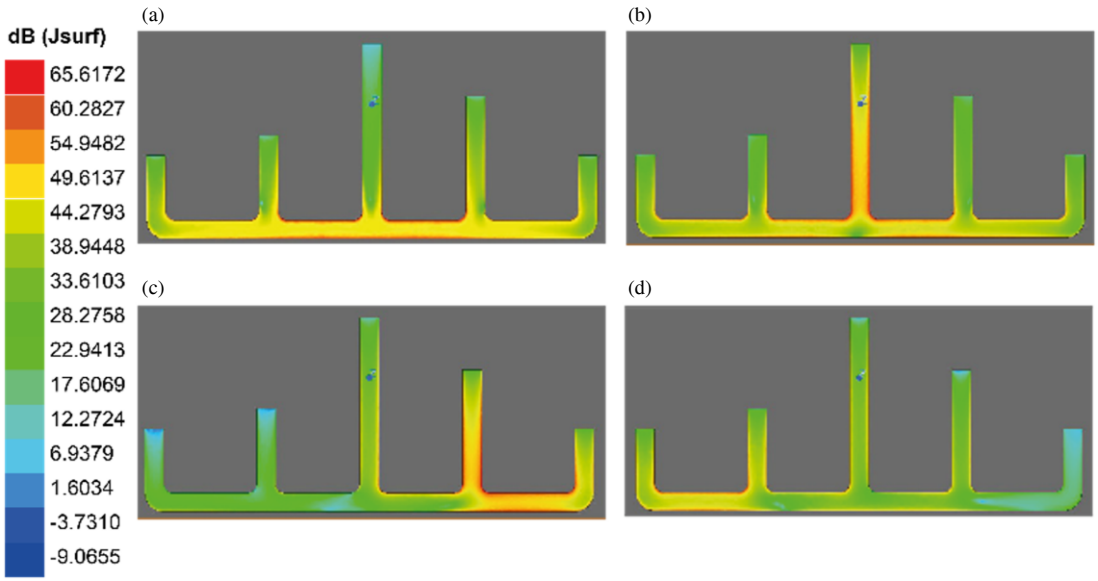

FIGURE 5. Current distribution in dB at (a) 2.45 GHz, (b) 3.5 GHz, (c) 5 GHz and (d) 5.8 GHz.

TABLE 1. Dimensions (in mm) of the proposed quadband NGD circuit.

Parameter	W	L	W_{TL}	L_{CL}	W_{CL}	S	H_0	H_1	H_2	H_3
Value	30.42	40.42	4.723	34.23	1.411	0.5	4.91	13.41	9.41	6.41

W_{CL}. The POC is simulated on Ansys®HFSS®. The dimensions used in the NGD circuit POC of Fig. 4 are presented in Table 1.

To address the BW behavior, better comprehension on the interaction of the stubs and the coupling effect is necessary. Before the NGD analysis, the interbranch coupling of each resonant mode will be investigated in the next subsection.

3.2. Surface Current Distribution Analyses of Resonant Modes

To evaluate the independence of each mode, the current distribution is analyzed. In Figs. 5(a)–(d), the region of higher current intensity for 2.45, 3.5, 5, and 5.8 GHz, respectively, is detailed.

It is perceptible that the path denoted by the current of each resonant mode is different, where the current at 2.45 GHz is concentrated at the base CL, the 3.5 GHz concentrated between the middle stub and base CL, the 5 GHz current defined by the path between the rightmost stubs, and the 5.8 GHz current defined by the leftmost ones. This is of utmost importance, since it allows the separate frequency tuning by modifying the width and length of the stubs with minor interference in the other resonant frequencies. The interaction between the stubs is evaluated in the following subsection by considering the procedure proposed in Subsection 2.4.

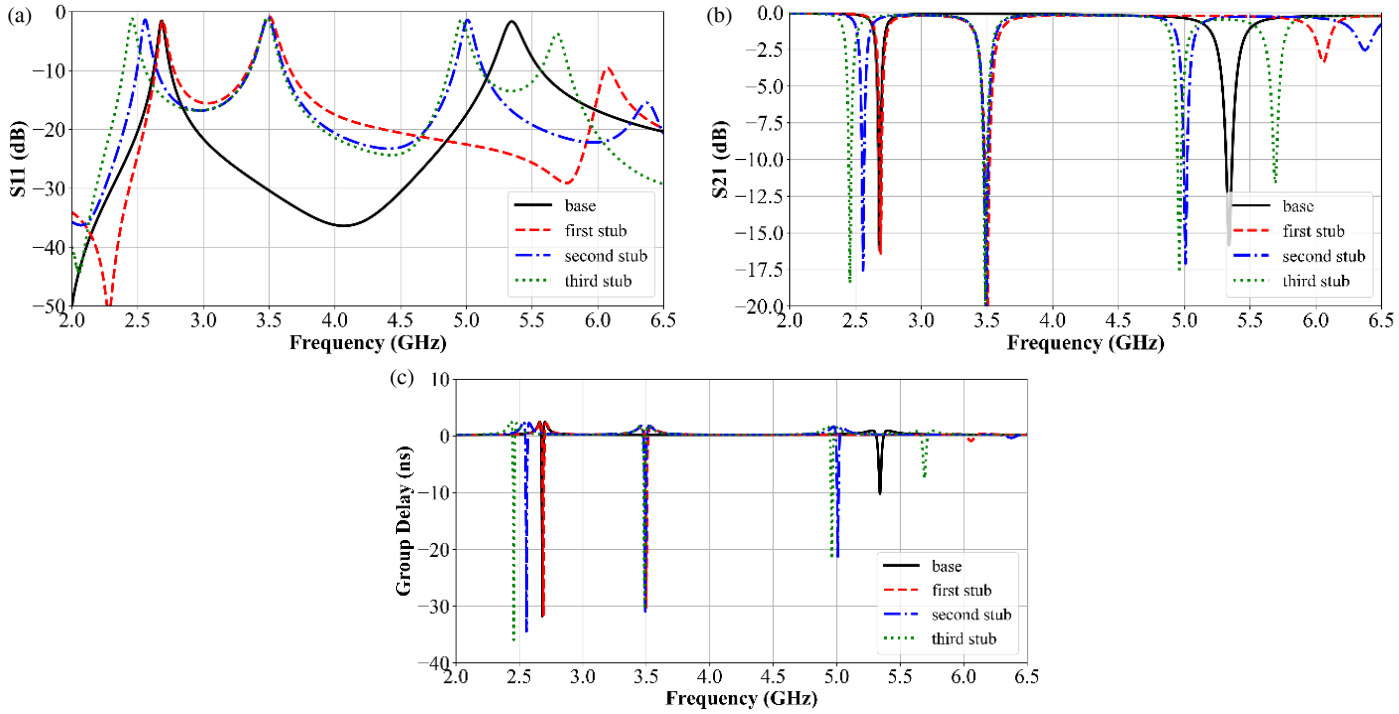

FIGURE 6. Results of the simulated quadband NGD circuit with each step: (a) S_{11}, (b) S_{21} and (c) GD.

3.3. WB Frequency Responses Showing the NGD Contribution Associated to Each Stub

Taking the model presented in Fig. 6 and starting with the base CL, the first (red), second (blue) and third (green) stubs are added in this order. The simulated results are shown in Fig. 6. It is seen that the base line corresponds to the Rejection Band (RB) at 2.69 GHz, while a second RB appears at 3.5 GHz when adding the first stub, with no change at the first RB perceived, mostly due to the distance between the stubs and the position of the new stub at the plane of symmetry of the filter. The insertion of the second and third stubs affects the first mode.

The hypothesis is that this effect is mostly due to the current dispersion of these stubs rather than the coupling between them and the outermost stubs. The addition of the third and fourth stubs reduces the first RB from 2.69 GHz to 2.45 GHz with the increase of the NGD effect. Furthermore, the second and third ones add 5.06 GHz and 5.73 GHz rejection bands, respectively, while the 3.5 GHz mode stays unchanged. The simulated and measured BWs can be calculated using (9), where f_0, f_2, and f_1 denote the center frequency, upper frequency, and lower frequency of the BW, respectively. At each frequency, it is observed that a BW is lower than 1%. The findings are summarized in Table 2.

TABLE 2. Results for the HFSS simulated quadband NGD circuit.

f_0 (GHz)	S_{21} (dB)	GD (ns)	BW (%)
2.457	−18.44	−35.94	0.89
3.487	−20.16	−30.52	0.83
4.962	−17.50	−21.65	0.66
5.691	−11.63	−7.47	0.97

These results diverge from what we derived in (10) due to the overlooking on the dielectric and conductive losses, which, from the theory on [31], shows that the BW is mainly controlled by the quality factor of the circuit, in other words, the relation between the reactive and resistive elements, although, for every bandwidth except the 5 GHz, the BWs fluctuate with low deviations.

4. PARAMETRIC ANALYSES OF QUADBAND NGD MICROSTRIP POC

This section studies the parametric analyses highlighting the influence of the circuit parameters.

4.1. Influence of CL Separation Space on NGD Responses

The separation parameter, S, varies from 0.25 mm to 0.75 mm with 0.05 mm steps, and the other variables from Table 1 are fixed. Fig. 7 provides a glimpse into the effect of the separation between the TL and crown topology. The blue/green stripes in Figs. 7(a)–(h) represent the NGD BW and filtering region, and the red stripes in Figs. 7(i)–(l) represent the higher reflection region of the circuit. As the filter topology gets closer to the TL, all bands deviate to upper values, as shown by the line bending to the right in Figs. 7(a)–(h). That means a change of resonant frequency to upper values, with special effect on the lowest band (2.428 GHz with a spacing of 0.75 mm to 2.529 GHz with a spacing of 0.25 mm), which presents a nonlinear transition. About the BW, it is perceptible by the line widening the increase of the S_{11} and S_{21} BWs in Figs. 7(c)–(h) and Figs. 7(i)–(l), respectively, when the CL comes closer to the TL, the same cannot be said about the GD BW, having a mod-

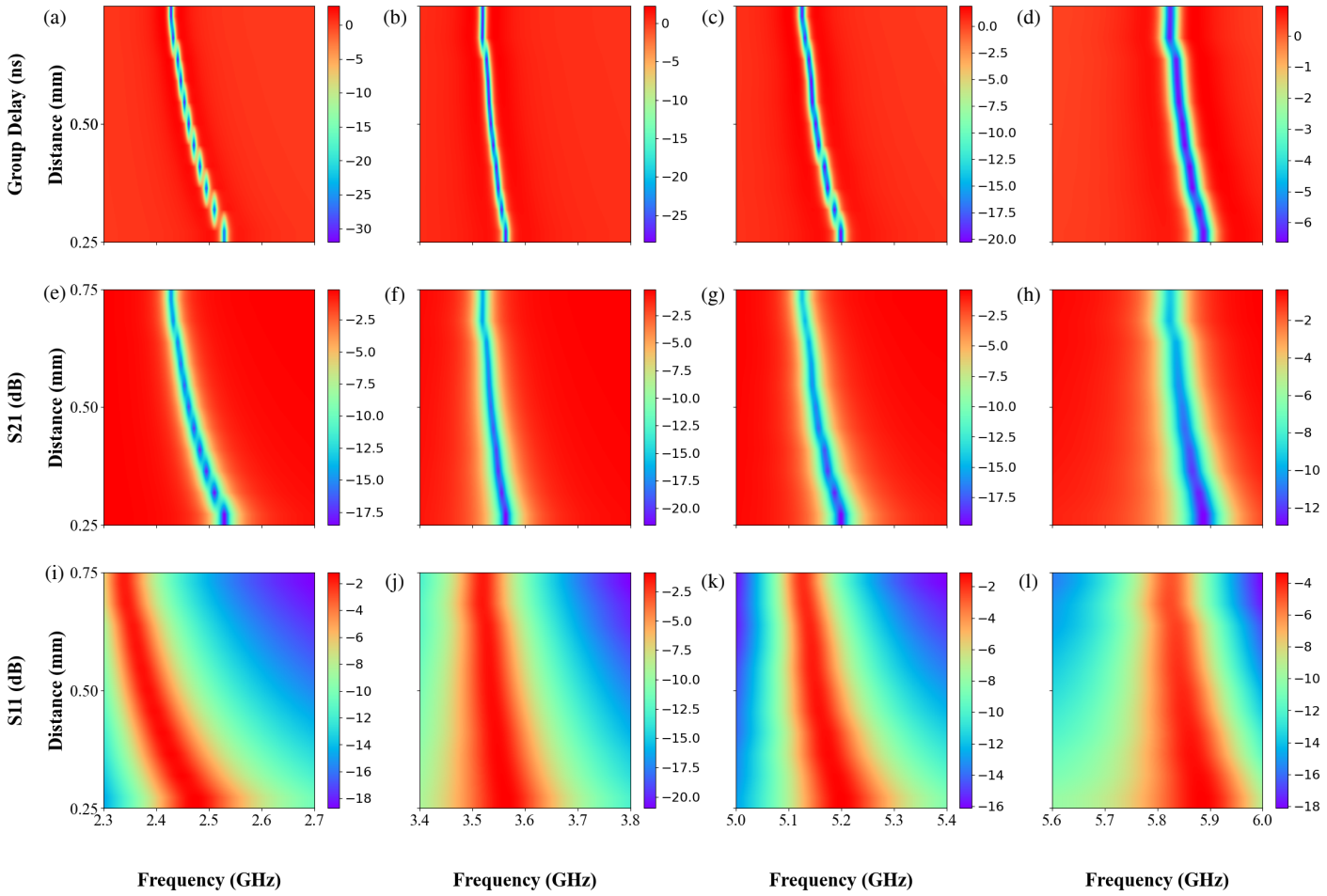

FIGURE 7. Effect of the distance between the TL and the CL. GD around (a) 2.3 GHz, (b) 3.5 GHz, (c) 5 GHz and (d) 5.8 GHz. S_{21} around (e) 2.45 GHz, (f) 3.5 GHz, (g) 5 GHz and (h) 5.8 GHz. S_{11} around (i) 2.45 GHz, (j) 3.5 GHz, (k) 5 GHz and (l) 5.8 GHz.

est increase throughout the analysis, going from 18.3 MHz at 2.428 GHz with $S = 0.75$ mm to 28.3 MHz at 2.529 GHz with $S = 0.25$ mm, although relatively, the BW increased 54.64%. These values in the center and extremes of the parameterization are summarized in Table 3. Another noteworthy point is that the ratio between two resonant frequencies is similar to the ratio between their BWs, showing the influence of the frequency as stated by (8).

4.2. Influence of Stub Physical Position on the Quadband NGD Responses

Each stub is repositioned ± 2 mm along the length of the CL using 0.5 mm steps for the parameterization. For the outermost stubs, i.e., the ones defining the base CL, it means a change in the overall length of the CL. The results of these parametric analysis are shown in Figs. 8 to 12. The stripes in the figures illustrate the resonant regions for the four bands of the circuit. When the leftmost stub is positioned to the left (positive variation), we see in Figs. 8(a)–(c) that all resonant frequencies are shifted to left (decreasing the center frequency of the affected modes) with exception of the 5 GHz BW.

The resonant frequency stays at 5.15 GHz as its main frequency and has a minor change in its maximum NGD, going from -20.54 ns at the position change of -2 mm to -19.85 ns at a position change of 2 mm, and S_{21} and S_{11} practically stay unchanged. This is coherent with Fig. 8(c), since the current is concentrated at the rightmost region.

The same analysis can be done to the rightmost stub as shown in Figs. 9(a)–(c), considering the inversion of direction, where the 5.8 GHz BW is poorly affected by this modification. For the inner stubs, as we change their positions, a symmetric response is perceived in Figs. 10 to 12. In Figs. 10 and 11, respectively, we see the shift of the center frequency to upper values denoted by the inner right (5.8 GHz) and left (5 GHz) stubs in a nonlinear fashion when they come close to the outermost stubs, mostly caused by the reduction of the current path.

As we see in Fig. 11, as the length of the left path becomes closer to the length of the right path, the last two modes tend to unite. Lastly, the middle stub brings a different behavior from the others, where it starts to decrease the center frequency from 3.6 GHz at the dislocation of -2 mm to 3.53 GHz at its original position, and then starts to increase again. The same can be said about the NGD which deviate its value from -25.83 ns at the 2 mm dislocation to -28.47 ns at the original position and shrink to -27.40 at the 2 mm dislocation. This effect can be explained due to the coupling of the middle stub with the other

TABLE 3. Summary of the TL and CL separation effect.

S (mm)	f (GHz)	S_{21} (dB)	S_{11} (dB)	GD (ns)	BW_{GD} (MHz)
0.25	2.529	−18.52	−1.19	−26.81	28.6
	3.563	−21.55	−0.88	−27.80	33.7
	5.199	−19.79	−1.10	−19.96	41.0
	5.887	−12.95	−3.35	−6.49	68.0
0.5	2.461	−16.68	−1.48	−31.09	21.4
	3.535	−18.67	−1.19	−28.31	27.3
	5.151	−16.55	−1.51	−20.09	32.3
	5.848	−10.85	−4.10	−6.35	56.0
0.75	2.428	−14.91	−1.84	−32.00	18.3
	3.519	−16.32	−1.55	−27.69	23.5
	5.125	−14.11	−2.00	−19.30	27.8
	5.825	−9.22	−4.92	−6.20	50.0

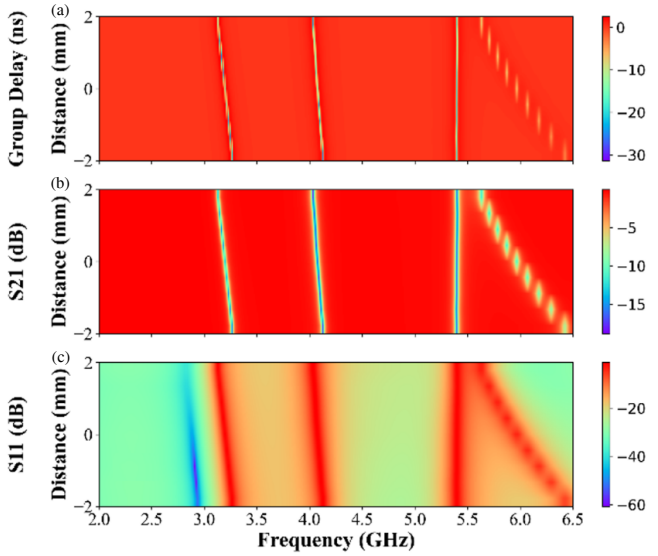

FIGURE 8. Effect of the reposition of the leftmost stub on (a) GD, (b) S_{21} and (c) S_{11}.

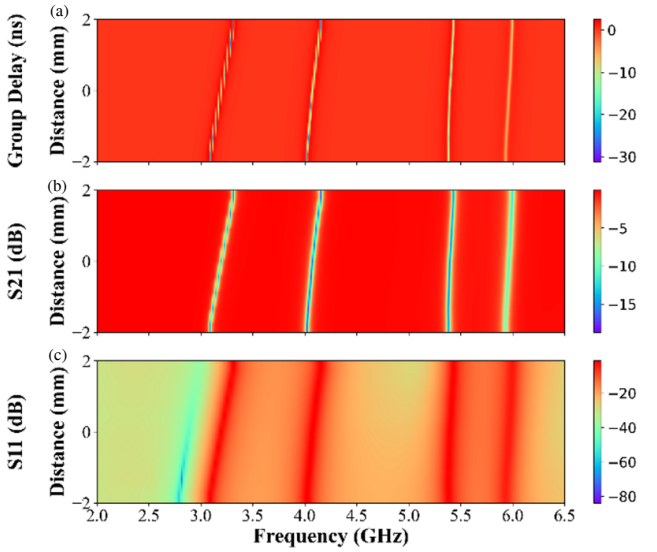

FIGURE 9. Effect of the reposition of the rightmost stub on (a) GD, (b) S_{21} and (c) S_{11}.

inner ones, as we see in the last two stripes an inverse response to the movement of the middle stub, when one deviates positively, and the other goes in the opposite direction.

4.3. Influence of Stub Widths on the Quadband NGD Responses

At this parameterization, only the inner stubs are changed since the outermost ones are part of the base CL. The stubs have its width changed from 0.411 mm to 2.411 mm while fixing its center position relative to the length of the circuit. In Fig. 13, we see that the change of the inner left stub causes a minor transition in the BWs of 2.45 GHz, 3.5 GHz, and 5 GHz. For 5.8 GHz, a higher transition is perceived, changing its center frequency from 5.73 GHz to 6.04 GHz while reducing its S_{21} and NGD from −13.03 dB and −9.33 ns to −7.11 dB and −2.89 ns, respectively.

For the middle stub, its parameterization has both a major effect for 3.5 GHz and a minor effect for 5 GHz and 5.8 GHz regions, as perceived in Fig. 14, but from Fig. 5(d), we can see that part of the current is presented on the center stub and near it, thus the aforesaid behavior is expected.

Lastly, the inner right stub modification has no effect on the 3.5 GHz and 5.8 GHz BWs, a minor effect on the 2.45 GHz, and a major effect on 5 GHz, as seen on Fig. 15.

In addition to the present parametric simulation analyses, the results of experimental validation are examined in the next section.

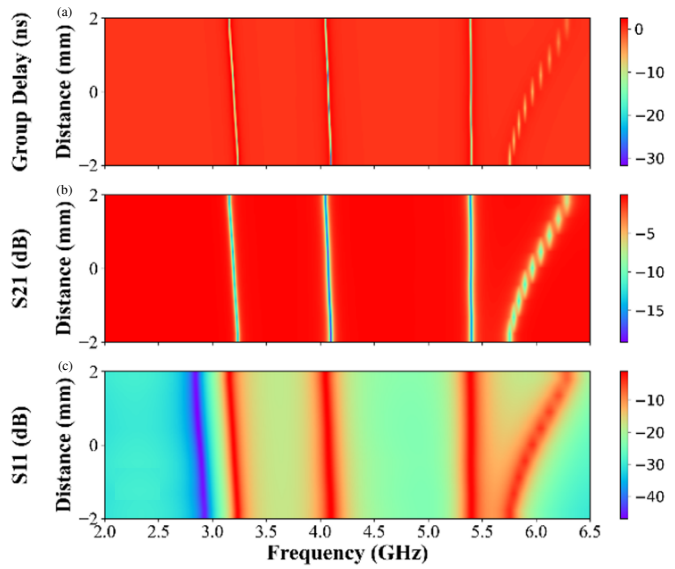

FIGURE 10. Effect of the reposition of the inner left stub on (a) GD, (b) S_{21} and (c) S_{11}.

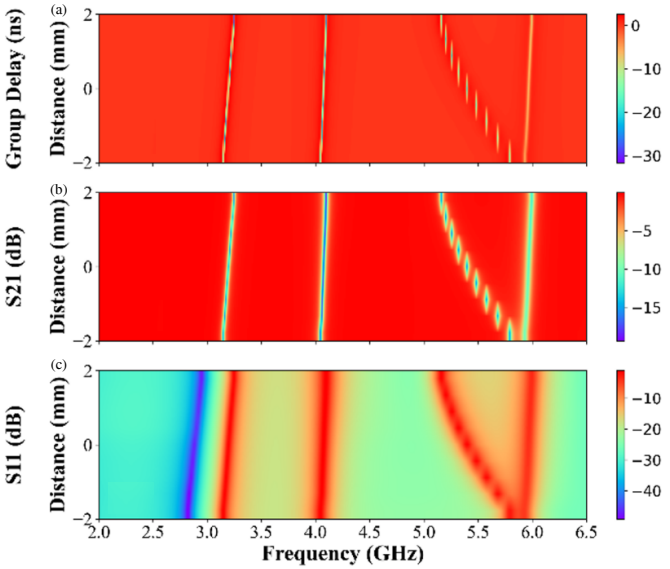

FIGURE 11. Effect of the reposition of the inner right stub on (a) GD, (b) S_{21} and (c) S_{11}.

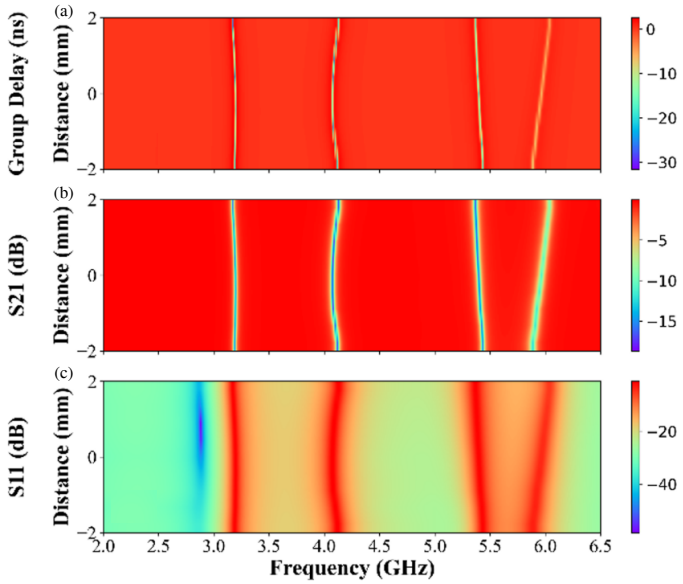

FIGURE 12. Effect of the reposition of the central stub on (a) GD, (b) S_{21} and (c) S_{11}.

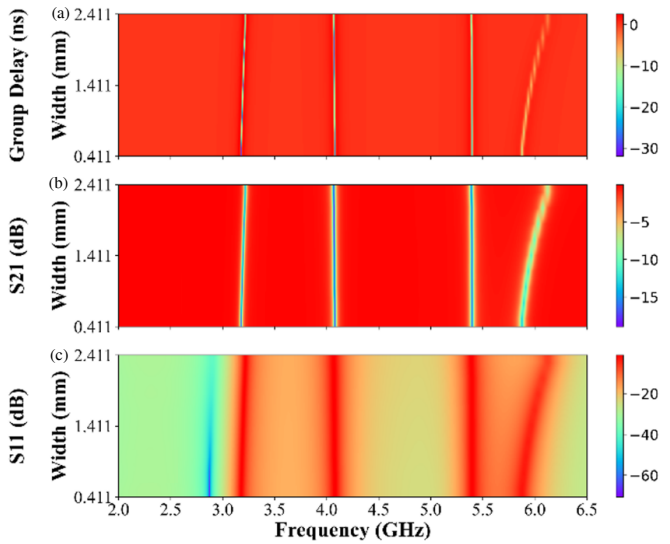

FIGURE 13. Changing width of the inner left stub and its influence on (a) GD, (b) S_{21} and (c) S_{11}.

5. DISCUSSION EXPERIMENTAL VALIDATION RESULTS SHOWING QUADBAND NGD MICROSTRIP DEMONSTRATOR

The quadband NGD function validation results based on the experimental measurement of the fabricated prototype is discussed in the present section.

5.1. Experimental Test Description of Quadband NGD Prototype

The constructed circuit is presented in Fig. 16(a). The circuit has an overall area of $0.45 \times 0.34\lambda_g^2$, where λ_g is the wavelength of a 2.45 GHz signal traveling at a 50 Ω TL set on the substrate. The circuit is measured with the Vector Network Analyzer (VNA) Rohde & Schwarz ZND, as depicted in Fig. 16(b).

The experimental test was performed to obtain its S_{21} and GD response at the 2 to 6.5 GHz band.

5.2. Measured and Simulated Results Confirming the Quadband NGD Validity

The comparison of the measured and simulated results is shown on Fig. 17. Except for the 5.8 GHz band, the simulated and measured results are in good agreement both for S_{21} and GD.

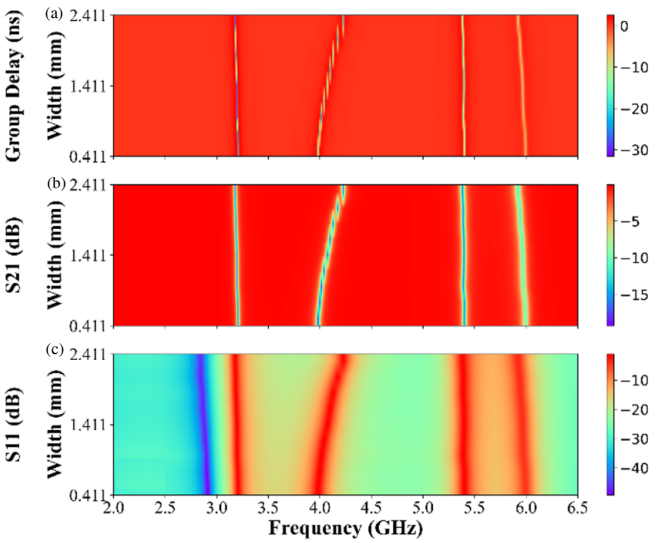

FIGURE 14. Changing width of the central stub and its influence on (a) GD, (b) S_{21} and (c) S_{11}.

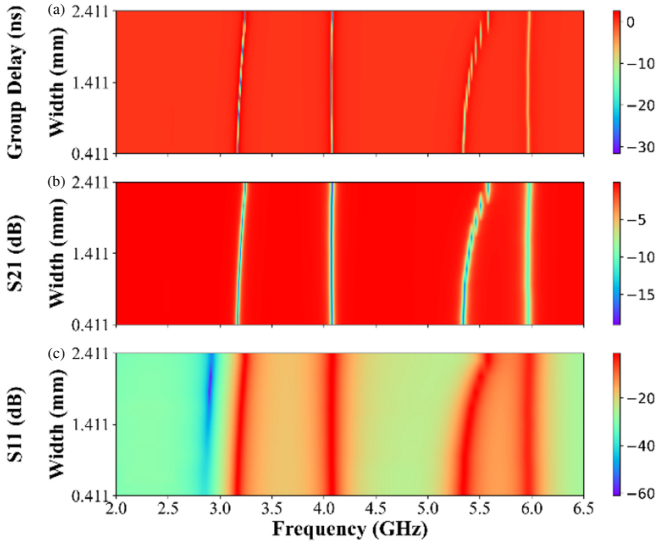

FIGURE 15. Changing width of the inner right stub and its influence on GD, (b) S_{21} and (c) S_{11}.

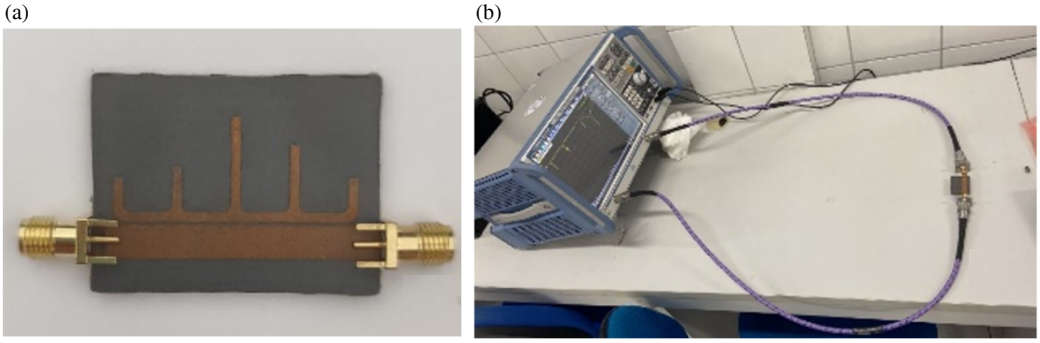

FIGURE 16. Photos of (a) quadband NGD circuit prototype and (b) measurement setup.

For all NGD regions, the deviations of the center frequency are under 2% based on the following relation:

$$\mathrm{BW_{NGD}}(\%) = 100 \times \frac{f_2 - f_1}{f_0} \tag{5}$$

where f_2 and f_1 are the higher and lower center frequencies. The measurement results are summarized in Table 4.

TABLE 4. Results for the measured quadband NGD circuit.

f_0 (GHz)	S_{21} (dB)	GD (ns)	BW (%)
2.415	−16.44	−30.6	0.87
3.477	−17.06	−24.15	0.77
5.057	−17.50	−15.57	0.67
5.728	−37.49	−43.61	0.59

To highlight the challenging performance of the tested quadband prototype, a comparative study will be discussed in the next subsection.

5.3. Comparative Study of Multiband NGD Circuits Available in the Literature

Using the most common figure of merit (FoM) [24, 27, 29] given by:

$$\mathrm{FoM} = |\tau(f_0)| \times BW_{NGD} \times |S_{21}(f_0)| \tag{6}$$

the proposed circuit along with the comparison presents a decrease of FoM by each frequency. In Table 5, a summary of the comparison of NGD characteristics and also the prototype physical size between the proposed circuit and the relevant recent literature [22, 24, 25, 27, 29] is presented. In this table, the NGD circuit physical size is chosen relatively to the wavelength λ_g because it is related the operating frequency.

It is noteworthy that the last NGD BW corresponding to $f_0 = 5.728$ GHz is penalized by its unexpectedly high IL. For the lowest frequencies, the circuit achieves a higher FoM than other models in literature:

(i) Ease of BW expansion by etching new stubs to the CL;

(ii) Only three degrees of freedom, namely the distance between the TL and CL, stub length, and stub width. This makes the fine tuning simpler;

TABLE 5. Comparison on the NGD characteristics and circuit size of this work to others in literature.

Ref	f_0 (GHz)	S_{21} (dB)	GD (ns)	BW (MHz)	NGD/IL (ns)	FoM	Tuning Variables	Size (λ_g) $L \times W$
[22]	2.13	−3.9	−5.9	19	3.7658	0.0715	10	0.74×0.49
	2.3	−3.4	−7.4	12	5.0030	0.0600		
	2.42	−2.4	−4.8	13	3.6412	0.0473		
[24]	1.23	−2.49	−1.60	18	1.2012	0.0216	10	0.41×0.30
	1.58	−3.55	−1.43	23	0.9502	0.0219		
[25]	1.54	−2.29	−1.84	23	1.4136	0.0325	9	0.92×0.46
	2.40	−3.59	−1.60	40	1.0583	0.0423		
	3.38	−4.78	−1.38	51	0.7959	0.0406		
	4.16	−5.70	−0.69	69	0.3580	0.0247		
[27]	2.03	−24.2	−3.65	19	0.2251	0.0043	13	0.17×0.30
	2.84	−27.3	−3.04	23	0.1312	0.0030		
[29]	1.76	−4.4	−1.85	58	1.1147	0.0647	12	0.23×0.36
	2.80	−7.8	−2.15	90	0.8759	0.0788		
	3.84	−9.7	−1.45	110	0.4746	0.0522		
	4.42	−9.3	−1.60	80	0.5484	0.0439		
	5.38	−8.9	−1.10	100	0.3948	0.0395		
This work	2.415	−16.44	−30.6	21	4.6102	0.0968	9	0.45×0.34
	3.477	−17.06	−24.15	27	3.3878	0.0915		
	5.057	−17.50	−15.57	34	2.0763	0.0706		
	5.728	−37.49	−43.61	34	0.5822	0.0198		

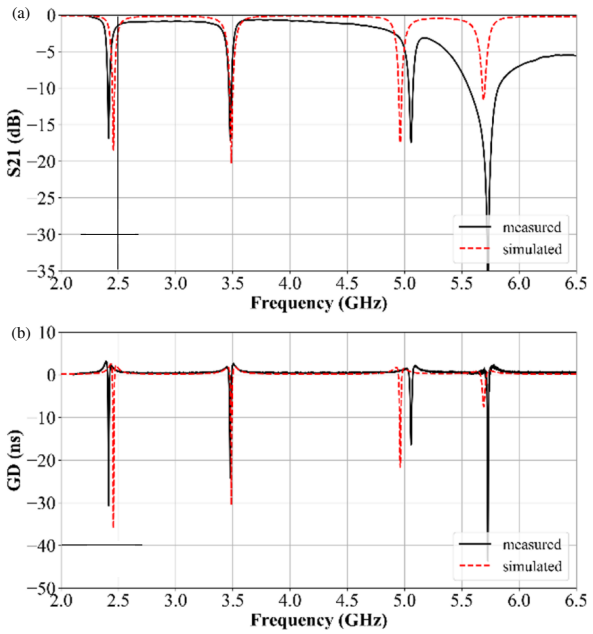

FIGURE 17. Comparison between measurement and simulation of (a) S_{21} and (b) GD.

(iii) Low interference between the modes;

(iv) Double BW by using a second CL etched to the other side of the TL as depicted in [24];

(v) And absence of lumped elements, which reduces the expected variability.

6. CONCLUSION

An innovative quadband NGD study of crown topology essentially constituted by TL stub and CL is developed. After the two-port topological description, the NGD analysis method is introduced. The analyses of all the geometric parameters from HFSS 3-D EM simulations on the NGD responses are discussed. Then, the proof of concept designed in microstrip topology is described in HFSS environment. A compact quadband NGD microstrip circuit based on CL able to operate in ISM band from 2 GHz to 6 GHz is designed, simulated, and measured.

The quadband NGD equivalent circuit is theoretically modeled from CL ladder topology. The circuit shows a simple structure to aggregate multiple NGD bands at the same structure with simple fine tuning and the extensibility of multiband effect by adding more stubs. As shown in Table 4, compared to other proposed methods in literature, this one achieves more NGD bands. Also, with the technique proposed in [24], the number of NGD bands can be doubled.

In the continuation of the present study, the quadband NGD topology is exploited for a myriad of applications such as:

- BP filter group delay equalization to alleviate the use of conventional and expensive techniques that insert more delay,
- Design of constant phase shifter for antenna arrays,
- The development of particularly innovative technique of EMI suppression in the RF and microwave systems.

ACKNOWLEDGEMENT

This study was financed in part by the Coordenação de Aperfeiçoamento de Pessoal de Nivel Superior — Brazil (CAPES) — Finance Code 001 and also supported in part by Natural National Science Foundation of China (NSFC) under Grant No. 62350610268.

REFERENCES

[1] Brillouin, L., *Wave Propagation and Group Velocity*, Academic Press, 2013.

[2] Chung, J.-Y., T. Yang, and J. Lee, "Low correlation MIMO antennas with negative group delay," *Progress In Electromagnetics Research C*, Vol. 22, 151–163, 2011.

[3] Mirzaei, H. and G. V. Eleftheriades, "Arbitrary-angle squint-free beamforming in series-fed antenna arrays using non-foster elements synthesized by negative-group-delay networks," *IEEE Transactions on Antennas and Propagation*, Vol. 63, No. 5, 1997–2010, May 2015.

[4] Zhu, M. and C.-T. M. Wu, "Reconfigurable non-foster elements and squint-free beamforming networks using active transversal filter-based negative group delay circuit," *IEEE Transactions on Microwave Theory and Techniques*, Vol. 70, No. 1, 222–231, Jan. 2022.

[5] Ravelo, B., G. Fontgalland, A. P. B. D. Santos, H. S. Silva, N. M. Murad, F. Haddad, M. Guerin, and W. Rahajandraibe, "Dual stopband type NGD network design for true time-delay based multi-beam steerer application," *Progress In Electromagnetics Research B*, Vol. 98, 107–123, 2023.

[6] Guerin, M., F. Haddad, W. Rahajandraibe, S. Ngoho, G. Fontgalland, F. Wan, and B. Ravelo, "BI-CMOS design of a*exp (-j *φ0) phase shifter as miniature microwave passive circuit using bandpass NGD resonant circuit," *Progress In Electromagnetics Research B*, Vol. 104, 1–19, 2024.

[7] Ravelo, B., M. Guerin, J. Frnda, F. E. Sahoa, G. Fontgalland, H. S. Silva, S. Ngoho, F. Haddad, and W. Rahajandraibe, "Design method of constant phase-shifter microwave passive integrated circuit in 130-nm BiCMOS technology with bandpass-type negative group delay," *IEEE Access*, Vol. 10, 93 084–93 103, 2022.

[8] Ravelo, B., G. Fontgalland, H. S. Silva, J. Nebhen, W. Rahajandraibe, M. Guerin, G. Chan, and F. Wan, "Original application of stop-band negative group delay microwave passive circuit for two-step stair phase shifter designing," *IEEE Access*, Vol. 10, 1493–1508, 2021.

[9] Meng, Y., Z. Wang, S.-J. Fang, and H. Liu, "Broadband phase shifter with constant phase based on negative group delay circuit," *Progress In Electromagnetics Research Letters*, Vol. 103, 161–169, 2022.

[10] Ravelo, B., M. Guerin, and W. Rahajandraibe, "Negative group delay predictor application for CO_2 gas concentration real-time forecasting," *IEEE Sensors Journal*, Vol. 24, No. 3, 3874–3887, Feb. 2024.

[11] Ravelo, B., M. Guerin, L. Rajaoarisoa, and W. Rahajandraibe, "Luminosity sensing application of negative group delay predictor," *IEEE Transactions on Industrial Electronics*, Vol. 71, No. 8, 9875–9885, Aug. 2024.

[12] Ravelo, B., F. Wan, Z. Yuan, and L. Rajaoarisoa, "Pre-detection sensing with multistage low-pass type negative group delay circuit," *IEEE Sensors Journal*, Vol. 22, No. 12, 11 835–11 846, Jun. 2022.

[13] Ravelo, B., M. Guerin, W. Rahajandraibe, and L. Rajaoarisoa, "All-pass NGD FIR original study for sensor failure detection application," *IEEE Transactions on Industrial Electronics*, Vol. 70, No. 9, 9561–9571, 2022.

[14] Chen, Z., J. Shi, and K. Xu, "Negative group delay power dividing network with balanced-to-single-ended topology," *IET Microwaves, Antennas & Propagation*, Vol. 13, No. 10, 1705–1710, Jun. 2019.

[15] Zhu, Z., Z. Wang, J. Zhou, T. Shao, S. Fang, and H. Liu, "Novel Gysel power dividers with negative group delay characteristics," *International Journal of Antennas and Propagation*, Vol. 2019, No. 1, 1564346, Aug. 2019.

[16] Nair, R. G. and S. Natarajamani, "Design theory of compact power divider with reconfigurable power division and negative group delay characteristics," *Scientific Reports*, Vol. 13, No. 1, 7222, May 2023.

[17] Chaudhary, G. and Y. Jeong, "Arbitrary power division ratio rat-race coupler with negative group delay characteristics," *IEEE Microwave and Wireless Components Letters*, Vol. 26, No. 8, 565–567, Aug. 2016.

[18] Zhang, A., J. Xu, and Z. Liu, "A microstrip linear-phase BPF using dual-band negative group delay equalizers," *IEEE Microwave and Wireless Technology Letters*, Vol. 34, No. 4, 387–390, Apr. 2024.

[19] Zhang, A., J. Xu, and Z. Liu, "Self-equalized linear-phase microstrip bandpass filter based on negative group delay parallel-coupled three-line units," *Microwave and Optical Technology Letters*, Vol. 66, No. 3, e34100, Mar. 2024.

[20] Zhang, A., J. Xu, and Z. Liu, "A self-equalized linear-phase absorptive BPF using negative-group-delay admittance inverters," *IEEE Microwave and Wireless Components Letters*, Vol. 32, No. 7, 851–854, Jul. 2022.

[21] Vauché, R., R. A. B. Mefteh, F. Haddad, J. Nebhen, W. Rahajandraibe, F. Wan, S. LALLéchère, and B. Ravelo, "Experimental time-domain study for bandpass negative group delay analysis with lill-shape microstrip circuit," *IEEE Access*, Vol. 9, 24 155–24 167, 2021.

[22] Wu, L., F. Wan, R. A. B. Mefteh, R. Vauché, G. Chan, X. Zhou, F. Haddad, W. Rahajandraibe, and B. Ravelo, "Innovative transient study of tri-bandpass negative group delay applied to microstrip barcode-circuit," *IEEE Access*, Vol. 9, 115 030–115 041, 2021.

[23] Zhou, X., Z. Gu, Q. Ji, X. Hu, R. Vauché, F. Haddad, N. M. Murad, J. Frnda, W. Rahajandraibe, F. Wan, and B. Ravelo, "Measurement characterization of band-pass NGD time domain of a 101O-topology passive circuit," *Radio Science*, Vol. 57, No. 4, 1–11, Apr. 2022.

[24] Wang, Z., S. Zhao, H. Liu, and S. Fang, "A compact dual-band differential negative group delay circuit with wideband common mode suppression," *IEEE Journal of Microwaves*, Vol. 2, No. 4, 720–725, Oct. 2022.

[25] Gu, T., J. Chen, B. Ravelo, F. Wan, V. Mordachev, and Q. Ji, "Quad-band NGD investigation on crossed resonator interconnect structure," *IEEE Transactions on Circuits and Systems II: Express Briefs*, Vol. 69, No. 12, 4789–4793, Dec. 2022.

[26] Palson, C. L., R. K. Sreelal, D. D. Krishna, and B. R. Jose, "Frequency switchable and tunable negative group delay circuits based on defected microstrip structures," *Progress In Electromagnetics Research M*, Vol. 113, 23–33, 2022.

[27] Yang, S., L. Zhang, Y. Chen, B. Li, and L. Wang, "Analysis of septuple-band NGD circuit using an E-shaped defected microstrip structure and two T-shaped open stubs," *IEEE Transactions on Microwave Theory and Techniques*, Vol. 70, No. 6,

3065–3073, Jun. 2022.

[28] Zhang, L., S. Yang, Q. Guo, H. Xiao, L. Wang, B. Li, and H. Zhang, "A compact passive quad-band negative group delay circuit with stepped impedance resonator and defected microstrip structure," *Radio Science*, Vol. 58, No. 1, 1–12, Jan. 2023.

[29] Zhang, L., D. Lu, S. Yang, Y. Chen, and B. Li, "Design of a quint-band passive NGDC by using Taguchi's optimization method," *AEU — International Journal of Electronics and Communications*, Vol. 171, 154921, Nov. 2023.

[30] Pozar, D. M., *Microwave Engineering*, Wiley, 2012.

[31] Ravelo, B., "Similitude between the NGD function and filter gain behaviours," *International Journal of Circuit Theory and Applications*, Vol. 42, No. 10, 1016–1032, 2014.

[32] Kandic, M. and G. E. Bridges, "Maximally flat negative group delay prototype filter based on capped reciprocal transfer function of classical bessel filter," *Progress In Electromagnetics Research B*, Vol. 110, 91–105, 2025.